Stability Frontiers and Mixed-Dimensional Physics in the Kagome Intermetallics Ln_3ScBi_5 (Ln = La–Nd, Sm)

Zhongchen Xu(徐忠琛)[1,2,3], Wenbo Ma(马文博)[2,3], Shijun Guo(郭世骏)[2,3], Ziyi Zhang(张孜毅)[2,3], Quansheng Wu(吴泉生)[3], Xianmin Zhang(张宪民)[1*], Xiuliang Yuan(袁秀良)[2,3*], and Youguo Shi(石友国)[2,3,4*]

[1]*Key Laboratory for Anisotropy and Texture of Materials (Ministry of Education), School of Material Science and Engineering, Northeastern University, Shenyang 110819, China*
[2]*Center of Materials Science and Optoelectronics Engineering, University of Chinese Academy of Sciences, Beijing 100190, China*
[3]*Beijing National Laboratory for Condensed Matter Physics and Institute of Physics, Chinese Academy of Sciences, Beijing 100190, China*
[4]*Songshan Lake Materials Laboratory, Dongguan 523808, China*

(Received 17 July 2025; accepted manuscript online 25 August 2025)

Low-dimensional physics provides profound insights into strongly correlated interactions, leading to enhanced quantum effects and the emergence of exotic quantum states. The Ln_3ScBi_5 family stands out as a chemically versatile kagome platform with mixed low-dimensional structural framework and tunable physical properties. Our research initiates with a comprehensive evaluation of the currently known Ln_3ScBi_5 (Ln = La–Nd, Sm) materials, providing a robust methodology for assessing their stability frontiers within this system. Focusing on Pr_3ScBi_5, we investigate the influence of the zigzag chains of quasi-one-dimensional (Q1D) motifs and the distorted kagome layers of quasi-two-dimensional (Q2D) networks in the mixed-dimensional structure on the intricate magnetic ground states and unique spin fluctuations. Our study reveals that the noncollinear antiferromagnetic (AFM) moments of Pr^{3+} ions are confined within the Q2D kagome planes, displaying minimal in-plane anisotropy. In contrast, a strong AFM coupling is observed within the Q1D zigzag chains, significantly constraining spin motion. Notably, magnetic frustration is partially a consequence of coupling to conduction electrons via Ruderman–Kittel–Kasuya–Yosida interaction, highlighting a promising framework for future investigations into mixed-dimensional frustration in Ln_3ScBi_5 systems.

DOI: 10.1088/0256-307X/42/10/100704 CSTR: 32039.14.0256-307X.42.10.100704

1. Introduction. In low-dimensional physical systems, the restricted paths for conducting electrons enhance interactions between particles, leading to strongly correlated interactions and enhanced quantum effects that are pivotal in the development of semiconductor devices,[1] topological insulators and quantum computing,[2,3] as well as superconductivity research.[4] The understanding of the strong correlation mechanism in quasi-one-dimensional (Q1D) materials, which consist of one-dimensional atomic chains or columnar moieties, is rooted in Luttinger Liquid theory,[5] describing electron behavior in one-dimensional conductors. Within these materials, Q1D spin chains coexist with inter-chain coupling, offering a versatile platform for investigating the magnetism of various models, including Ising,[6] Heisenberg,[7] and XY-type models.[8] Moreover, highly frustrated quasi-two-dimensional (Q2D) kagome lattice magnets are characterized by geometric frustration and unique electronic structures, which can give rise to various intriguing quantum states. Vanadium-based kagome materials AV_3Sb_5 (A = K, Rb, Cs) exhibit a range of exotic phenomena including superconductivity, anomalous Hall effect and electronic nematicity.[9–11] The distorted kagome intermetallic compound CePdAl manifests a paramagnetic quantum-critical phase due to the competitive interplay of geometric frustrations, Ruderman–Kittel–Kasuya–Yosida (RKKY) interactions, and Kondo effects.[12] The exploration of complex magnetic ground states and quantum transport arising from the interplay of Q1D and Q2D hybrid low-dimensional characteristics in a system is an intriguing endeavor.

The Ln_3ScBi_5 family (Ln = La–Nd, Sm) has attracted our research interest, as it simultaneously hosts Q1D zigzag spin chains and Q2D distorted kagome motifs, making it an excellent candidate for studying mixed-dimensional frameworks. The hypervalent bismuthide La_3ScBi_5 is distinguished by its unique 1D bismuth chains, which have given rise to unusual phenomena including quasi-linear magnetoresistance, quantum oscillations, and paramagnetic singularity.[13] The frustrated Q2D Kondo-lattice compound Ce_3ScBi_5 exhibits interactions with crystal electric field (CEF) splitting, Kondo scattering, and RKKY interaction at closely related energy scales, leading to the emergence of fractional magnetization plateaus and singular anisotropic transport.[14] For the Ln_3ScBi_5

*Corresponding authors. Email: zhangxm@atm.neu.edu.cn; yuanxiuliang8@iphy.ac.cn; ygshi@iphy.ac.cn
© 2025 Chinese Physical Society and IOP Publishing Ltd. All rights, including for text and data mining, AI training, and similar technologies, are reserved.

system, it is of significant physical importance to explore the synthesis of heavier rare earth elements to investigate the stability frontiers and analyze the common features induced by the mixed-dimensional structure across the system.

In this study, we successfully optimized the flux-growth synthesis conditions and systematically synthesized a series of high-quality single crystals exhibiting anti-Hf_5Sn_3Cu-type hexagonal structures from the Ln_3ScBi_5 family. Through a comprehensive analysis, the structural diversity and stability boundaries within this family were visualized and evaluated. Special attention is given to Pr_3ScBi_5, where we investigate the influence of the zigzag chain of Q1D and the kagome layer of Q2D in the mixed-dimensional structure on its magnetic ground state. The ordered magnetic moments of the non-collinear Pr^{3+} ions are confined to the Q2D kagome plane, exhibiting minimal in-plane anisotropy, while strong AFM coupling is observed in the Q1D zigzag chains, where spin motion is significantly constrained. These unique features can also be extended to the Ln_3ScBi_5 family. It is worth noting that the magnetic entropy at the antiferromagnetic (AFM) transition is significantly reduced, and that the transition occurs at a lower temperature below the wide peak of magnetic susceptibility, indicating pronounced spin fluctuations in Pr_3ScBi_5. The Ln_3ScBi_5 system serves as a paradigm for further investigating the interplay between spin frustration and RKKY interaction across mixed dimensions.

2. Methods.

2.1. Optimized Flux Single-Crystal Growth. Millimeter-scale single crystals of Ln_3ScBi_5 were synthesized using a self-flux method. Rare earth (Ln) lumps were physically polished to remove the oxide layer, then weighed together with scandium (Sc) pieces and bismuth (Bi) balls at a certain molar ratio. The precise ratio of Ln:Sc:Bi is flexible; reproducible and optimal ratios were experimentally determined: Pr:Sc:Bi = 1:4:10, Nd:Sc:Bi = 1:4:10, and Sm:Sc:Bi = 1:3:5. The reagents were placed in a 5 ml Al_2O_3 crucible containing a connecting crucible, sealed in a fused silica tube under approximately 0.6 atm of argon gas. The samples were heated to 1000–1050 ℃ over 10 hours, held at this temperature for 18 hours, then slowly cooled at a rate of 1–1.5 ℃/h to 700 ℃, followed by centrifugation at 700 ℃.

Ln_3ScBi_5 single crystals exhibit a typical hexagonal morphology. Residual Bi flux on the crystal surfaces was removed using a scalpel, revealing a lustrous silver appearance. Crystal size is constrained by the volume of the growth container. Members of the Ln_3ScBi_5 family yield samples with average centimeter-scale dimensions, with the exception of Sm_3ScBi_5, which forms slender filaments or strips, with an average size of only $0.5 \times 0.5 \times 5$ mm^3. These single crystals exhibit air sensitivity, necessitating both their subsequent storage and preparation to be conducted within an argon-filled glove box.

2.2. Characterizations. The diffraction peaks corresponding to the (h00) surfaces of single crystals were measured using a Bruker D2 phaser detector with Cu Kα radiation. Single crystals of Ln_3ScBi_5 were mounted on kapton loops with Paratone oil for single-crystal X-ray diffraction (XRD) data collection. Diffraction data were collected at 274(2) K on a Bruker D8 VENTURE PHOTON II diffractometer using Mo Kα radiation (λ = 0.71073 Å). Structure solutions were obtained using intrinsic phasing methods with the APEX4 software, and the crystal structure was refined using a full-matrix least-squares method on F^2 with the SHELXL-2018/3 program. The chemical composition of the as-grown crystals was determined using energy-dispersive X-ray spectroscopy in a Hitachi S-4800 scanning electron microscope at an accelerating voltage of 15 kV.

2.3. Physical Properties Measurement. Temperature-dependent susceptibility was conducted from 2 to 300 K using a Magnetic Properties Measurement System (MPMS, Quantum Design) with varied applied fields in the zero-field-cooling (ZFC) and field-cooling (FC) modes. Isothermal magnetization was assessed on the MPMS (7 Tesla) and a Physical Properties Measurement System (PPMS, Quantum Design, 16 Tesla), utilizing a vibrating sample magnetometer option. Electrical transport measurements were performed on the PPMS (up to 9 Tesla) using the standard four-probe technique built by platinum wire and silver epoxy with current applied along the c-axis. The resistance signals were obtained by symmetrizing the data collected in reversed magnetic fields. Heat capacity was measured in the PPMS using its specific heat option, employing a thermal relaxation method. The addenda data were measured in advance, and the temperature-rise parameter was set to a minimal value of 1% to achieve the best temperature resolution.

3. Results and Discussion.

3.1. Ln_3ScBi_5 Structural Trends. Ln_3ScBi_5 crystallizes in an anti-Hf_5Sn_3Cu-type hexagonal structure, which can alternatively be interpreted as an interstitial derivative of the Mn_5Si_3-type structure. In this framework, the rare-earth atom occupies the single Wyckoff site 6g, Sc resides the site 2b, and Bi is distributed across two distinct sites: Bi1 at 6g and Bi2 at 4d. This specific arrangement leads to an anisotropic environment where Sc is coordinated by octahedra of Bi1, which share faces along the hexagonal c[0001] direction [Fig. 1(a)]. The structure of Ln_3ScBi_5 exhibits a unique mixed-dimensional characteristic, featuring Q1D zig-zag chains of rare-earth atoms aligned along the c-axis [Fig. 1(b)] and Q2D distorted kagome layers, symmetrically stacked through the 6_3 screw axes of Sc atoms within the ab-plane [Fig. 1(c)]. The incorporation of such mixed-dimensional elements, together with the coexistence of rare-earth metal magnetism, can foster a rich spectrum of exotic quantum phenomena.

Crystals of Ln_3ScBi_5 grown from a bismuth self-flux exhibit a bright, silver luster and are mechanically soft, allowing for easy cleavage. As an illustrative example, further characterization and analysis were performed on a single crystal of Pr_3ScBi_5. Figure 1(d) displays the XRD pattern of the single crystal plane, where (h00) peaks are prominently observed, and the rod-shaped sample extends along the c-axis. Figure 1(e) presents reconstructed

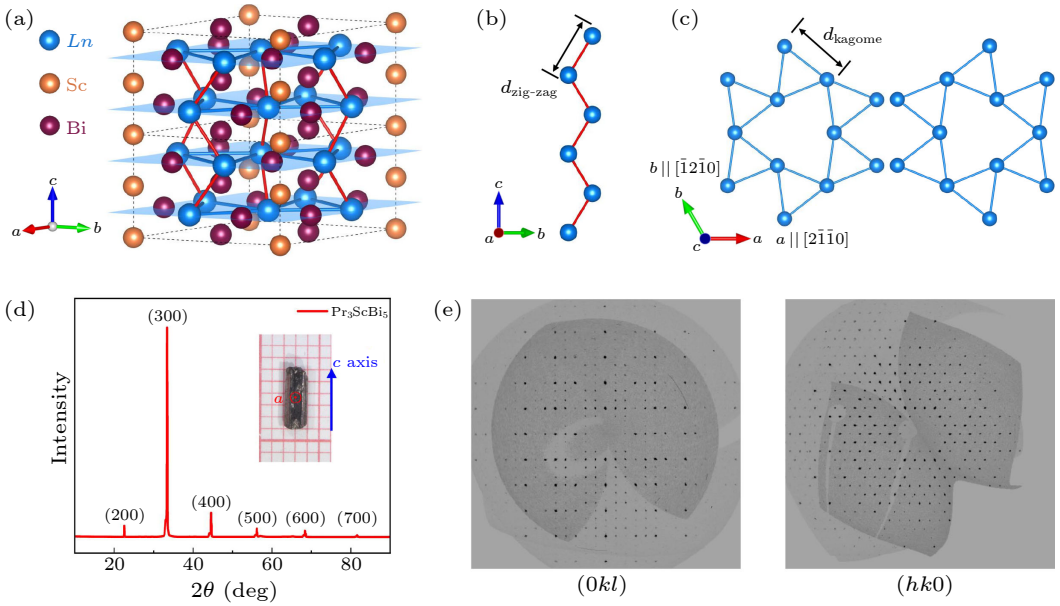

Fig. 1. Schematic crystalline structure of the Ln_3ScBi_5 family, utilizing Pr_3ScBi_5 single crystal as an example for characterization. (a) Overall crystal structure of Ln_3ScBi_5 showcases Q1D zig-zag chains along (b) the c-axis direction, exhibiting a Q2D distorted kagome lattice in the ab plane, and a stacking arrangement along (c) the crystallographic 2_1 screw axis. (d) XRD θ–2θ scan of a flat surface of Pr_3ScBi_5 single crystals. (e) Reconstructed single-crystal XRD patterns of $(0kl)$ and $(hk0)$ reflection planes, respectively.

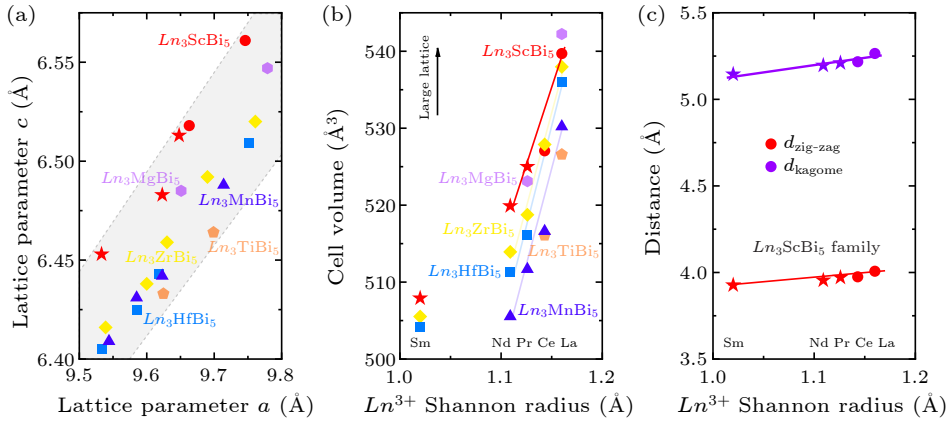

Fig. 2. Stability frontiers of the Ln_3ScBi_5 family. (a) Plot of the a and c lattice parameters for all currently known Ln_3MBi_5 (Ln = La–Nd, Sm; M = Sc, Mg, Ti, Zr, Hf) compounds.[13–24] The five-pointed star symbolizes the recently synthesized compound in this study, signifying an expansion of the system. (b) Schematic of phase stability across the lanthanide row. The coordination of Ln is approximately VIII-coordinate in the Ln_3MBi_5 structure. (c) Nearest-neighbor distance between Nd atoms in zig-zag chains and kagome layers in the Ln_3ScBi_5 family, extracted from SCXRD results and plotted against the VIII-coordinate Shannon ionic radius.

single-crystal XRD patterns of $(0kl)$ and $(hk0)$ reflection planes, respectively, measured at 274 K. Comprehensive details regarding CIF files, refinement parameters, and additional characterization are provided in Tables S1–S3 and Fig. S1 of the Supplementary Materials (SM).

The intricate connection between the size of the filler atoms and the host lattice results in their robust structure and tunable diversity within the Ln_3ScBi_5 and related systems. To illustrate this, the lattice parameters a and c for known Ln_3MBi_5 compounds have been plotted, as shown in Fig. 2(a).[13–24] The overall trend is visually striking; the Ln_3ScBi_5 family exhibits an extended lattice parameter c, which can be attributed to the larger combined metal radii of Sc and Bi atoms within their octahedral configurations. Furthermore, the lattice parameter a of Ln_3ScBi_5 is slightly smaller than that of Ln_3MgBi_5, resulting in a similar unit cell volume between the two systems [Fig. 2(b)]. In contrast to the usual lanthanide trend, when rare earth atoms shrink, the Ln_3MBi_5 series deviates from the typical linear trend observed in rare earth substitution series.[25] As smaller rare earth elements are incorporated, the rate of volumetric contraction within the lattice progressively diminishes, which is attributed to the resistance of M-Bi bonds within octahedron to further compression.

Through systematic and comprehensive experimental

investigations, the stability boundary of Ln_3ScBi_5 can be elucidated from multiple perspectives with enhanced depth. When the Shannon radius of rare earth elements is reduced to that of Sm^{3+} ions, the synthesis of high-quality Sm_3ScBi_5 single crystals becomes highly challenging: the yield of single crystals is extremely low, and they predominantly form long, slender filaments. This is attributed to the significant radius difference between charge balancing sublattices, which increases structural instability and hampers single crystal growth,[26] as corroborated by the volume deviation of Sm_3ScBi_5 from the linear trend in Fig. 2(b). When employing smaller rare earth species such as Gd^{3+}, Er^{3+}, and Lu^{3+}, the preferential precipitation of the Ln_3ScBi_5 phase is inhibited, leading to the predominant formation of a simple rock-salt structure featuring Sc-doped $Ln_{1-x}Sc_xBi$.

Figure 2(c) makes a detailed comparison of the nearest neighbor distances within the zig-zag chains of Q1D motifs and within the distorted kagome layers of Q2D networks in the Ln_3ScBi_5 system. Despite the significant variation in the Shannon radius of rare earth elements, the responses of $d_{\mathrm{zig-zag}}$ and d_{kagome} in Ln_3ScBi_5 are comparatively modest, with both $d_{\mathrm{zig-zag}}$ being substantially shorter than d_{kagome}, which indicates that the nearest neighbor distance of rare earth elements falls within the Q1D zig-zag chains. The RKKY interaction mediates long-range magnetic exchange in the intermetallic compound Ln_3ScBi_5, potentially stabilizing a diverse range of quantum ground states within its geometrically frustrated Q2D lattices.[27] By employing Pr_3ScBi_5 single crystals as a design paradigm, we explore the exotic spin fluctuations and diverse magnetic ground states induced by complex structural mixed dimensionality in the Ln_3ScBi_5 system.

3.2. Frustrated Kagome-lattice AFMs. The summary chart of the physical properties of Pr_3ScBi_5 varying with temperature is shown in Fig. 3, highlighting a strong correlation between electrical transport and magnetic order. The electrical resistivity $\rho_{\parallel}(T)$ of Pr_3ScBi_5 for $H \parallel [2\bar{1}\bar{1}0]$ decreases monotonically with decreasing temperature, showing metallic behavior [Fig. 3(a)]. The large residual resistivity ratio ($RRR = \rho_{\parallel}(300\,\mathrm{K})/\rho_{\parallel}(2\,\mathrm{K}) \approx 11.9$) suggests that the as-grown crystals are of excellent quality and that the results are reproducible. The magnetic component of electrical resistivity $\rho_{\mathrm{mag}}(T)$, estimated by subtracting phonon contributions using the $\rho_{\parallel}(T)$ data of La_3ScBi_5 [Fig. 3(b)], exhibits a $-\log T$ dependence in the temperature ranges $110\,\mathrm{K} \le T \le 300\,\mathrm{K}$ and $20\,\mathrm{K} \le T \le 90\,\mathrm{K}$, and shows the emergence of a broad hump around 100 K. This behavior can be attributed to Kondo-type interaction in the presence of strong CEF splitting, with the Kondo temperature being much lower than the overall crystal field splitting.[28,29] Caution is warranted when attributing resistivity changes to magnetic effects via curve subtraction, as impurity scattering variations between samples may obscure interpretation. Notably, the resistivity undergoes a significant decrease below $T_{\mathrm{N}} = 5.1\,\mathrm{K}$, indicating the onset of magnetic ordering in Pr_3ScBi_5, which results in a reduction of magnetic scattering. The bulk nature of the magnetic transition observed in transport measurements is confirmed by the λ-shaped peak with appreciable magnitude near T_{N} in the $C_{\mathrm{p}}(T)$ curve. The zero-field C_{p} data in the temperature range from 1.8 to 200 K were analyzed using a combination of Debye and Einstein models[30] according to

$$C_{\mathrm{p}} = \gamma^{\mathrm{DE}}T + 9nR\alpha\Big(\frac{T}{T_{\mathrm{D}}}\Big)^3\int_0^{\frac{T_{\mathrm{D}}}{T}}\frac{x^4\mathrm{e}^x\mathrm{d}x}{(\mathrm{e}^x-1)^2} + 3nR(1-\alpha)\Big(\frac{T_{\mathrm{E}}}{T}\Big)^2\frac{\mathrm{e}^{\frac{T_{\mathrm{E}}}{T}}}{\Big(\mathrm{e}^{\frac{T_{\mathrm{E}}}{T}}-1\Big)^2}. \quad (1)$$

The optimal fitting of the yield parameters $\gamma^{\mathrm{DE}} = 51.0\,\mathrm{mJ{\cdot}mol_{Pr}^{-1}{\cdot}K^{-2}}$, $T_{\mathrm{D}} = 168.98\,\mathrm{K}$ and $T_{\mathrm{E}} = 22.28\,\mathrm{K}$ indicates a moderately enhanced electronic Sommerfeld coefficient, considerably larger than $\gamma^{\mathrm{DE}} = 5.88\,\mathrm{mJ{\cdot}mol_{La}^{-1}{\cdot}K^{-2}}$ observed in La_3ScBi_5. By contrast, the low temperature C_{p}/T–T^2 data from 1.8 to 25 K was well described by Debye's description $C/T = \gamma + \beta T^2$, yielding $\gamma^{\mathrm{D}} = 43.5\,\mathrm{mJ{\cdot}mol_{La}^{-1}{\cdot}K^{-2}}$ and $\beta = 1.73\times10^{-3}\,\mathrm{J{\cdot}mol^{-1}{\cdot}K^{-4}}$. The two models obtained similar Sommerfeld coefficients, which demonstrated the rationality of data fitting from multiple perspectives, pointing to a slight enhancement in the effective mass and the existence of partial hybrid f-electron states.[31] The magnetic specific heat divided by temperature of Pr_3ScBi_5, illustrated in Fig. 3(d) as a function of $\log T$, exhibits two distinct features: a jump around T_{N} and a broad maximum around 10 K. The latter may correspond to the Schottky anomaly arising from the thermal variation of the 4f CEF energy levels.[32] The magnetic entropy S_{m} reaches only $28\% \times 3R\ln 2$ at T_{N} and increases up to $3R\ln 2$ by 15 K, which suggests a quasi-doublet ground state. The considerably reduced entropy relative to $R\ln 2$ is consistent with the presence of spin fluctuations at temperatures higher than T_{N}, as reflected by the moderately γ^{D} value estimated from paramagnetic regime.

The magnetic susceptibility $\chi(T)$ was measured in an external field of 1 kOe applied along the $[2\bar{1}\bar{1}0]$ and [0001] directions, as depicted in Fig. 3(e). Both $\chi(T)$ curves exhibit no discernible distinction between ZFC and FC and feature a sharp peak around 5.1 K, indicative of AFM ordering of the Pr^{3+} moments. Throughout the entire temperature range, the $\chi(T)$ value at $H \parallel [2\bar{1}\bar{1}0]$ is one order of magnitude greater than that at $H \parallel [0001]$. This significant magnetic anisotropy is widespread in the Ln_3ScBi_5 system, indicating that the ordered moments of rare-earth atoms are aligned within the *ab*-plane. The inverse magnetic susceptibility, $\chi^{-1}(T)$, depicted in Fig. 3(f), accurately follows the Curie–Weiss law. The estimated effective moments for $H \parallel [2\bar{1}\bar{1}0]$ and $H \parallel [0001]$ are $3.786\,\mu_{\mathrm{B}}$ and $3.757\,\mu_{\mathrm{B}}$, respectively, both of which are close to the theoretical value of the free Pr^{3+} ion. The distinct Weiss temperatures of 5.507 K (in-plane) and −106.35 K (out-of-plane) highlight the strong magnetic crystal anisotropy of Pr^{3+} as governed by CEF.[33] In the Ln_3ScBi_5 system (excluding the non-magnetic element La), where AFM interactions prevail, the Q2D distribution of rare earth atoms within the *ab*-plane strongly influences AFM order driven by synergistic interplay between CEF confinement and magnetic frustration.

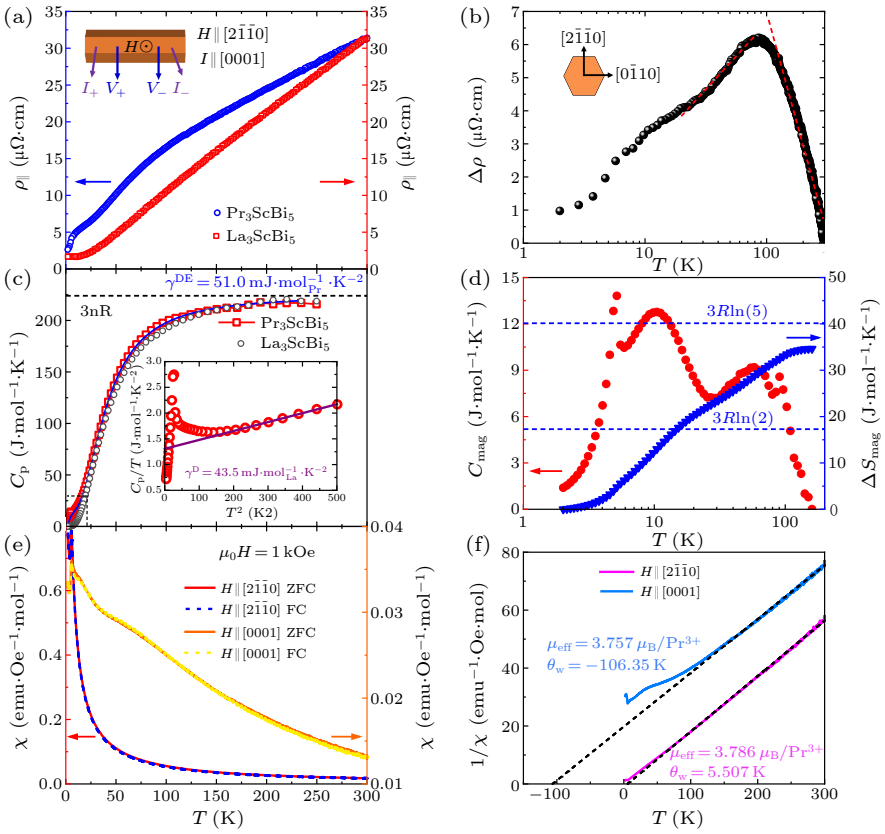

Fig. 3. Summary chart of temperature-dependent physical properties of Pr_3ScBi_5. (a) Temperature-dependent resistivity of Pr_3ScBi_5 and its nonmagnetic analog La_3ScBi_5 in zero field, measured for the current flowing along the c-axis. (b) Resistivity induced by the magnetism of Pr^{3+} ions. The dashed straight line indicates the logarithmic slope of the resistivity. (c) Temperature-dependent specific heat of Pr_3ScBi_5 and La_3ScBi_5. The blue curve represents the Debye–Einstein fitting. The inset depicts the low-temperature C_p/T vs T^2 behavior, with the purple line representing the Debye model linear fit. (d) Specific heat and entropy associated with the magnetic component. (e) Temperature variation of magnetic susceptibility measured in a magnetic field of $\mu_0 H = 1$ kOe applied parallel to $[2\bar{1}\bar{1}0]$ ([100] a-axis) and [0001] ([001] c-axis) directions. ZFC and FC data are shown by solid lines and dashed lines, respectively. (f) Curie–Weiss fit to the magnetic susceptibility data.

3.3. Evolution of AFM Order with Field Variation. Figure 4(a) displays the $\rho_\parallel(T)$ curves, measured below 50 K under various magnetic fields applied along the $[2\bar{1}\bar{1}0]$ direction. As the magnetic field increases, the resistivity decrease near T_N systematically broadens and shifts to lower temperatures, eventually vanishing at 30 kOe (Fig. S4a of the SM), leading to a pronounced positive magnetoresistance (discussed further below). C_p/T versus T curves, depicted in Fig. 4(b), provide additional insights into the thermodynamic aspects of the magnetic correlations and behavior in Pr_3ScBi_5. The peak associated with T_N shifts to lower temperatures with increasing field and disappears at $H = 20$ kOe, which is a typical characteristic fingerprint of the AFM transition.

Consistent with the potential enhancement of spin fluctuations in Pr_3ScBi_5, the magnetic susceptibility within the basal plane, $\chi(T)$ along the $[2\bar{1}\bar{1}0]$ direction, exhibits a broad maximum at $T_{max} > T_N$ and an abrupt drop at T_N upon further cooling, as is corroborated by a sharp peak of $d\chi/dT$ (Fig. S4b of the SM) and C_p/T versus T data. These intriguing features indicate that although the static magnetic susceptibility begins to decline at T_{max}, the dynamic magnetic susceptibility continues to increase below T_{max} due to spin frustration caused by the Q2D kagome-like structure in Ln_3ScBi_5, ultimately leading to the emergence of a long-range AFM order.[34] This distinctive magnetic behavior is also observed in other compounds within the Ln_3ScBi_5 system, indicating a universal influence of spin frustration on magnetic ordering. In addition, at temperatures lower than T_N, the $\chi(T)$ curve reaches a local minimum at T_{min} and subsequently exhibits a pronounced upward rise. This increase in $\chi(T)$ curves is attributed to the hyperfine sensitivity of the Pr^{3+} nuclear spins, which arises due to the large hyperfine field generated by 4f electrons characterized by significant Van Vleck magnetic susceptibility.[35] Based on this analysis, in the Ln_3ScBi_5 system, geometry of rare earth atoms causes magnetic frustration even though these atoms are far enough apart from one another that direct exchange is most likely not present; thus, this system relies on RKKY type long-range interactions which typically cause impacts from geometrically frustrated lattices.

For $H \parallel [0001]$, the magnetic susceptibility curve is approximately one order of magnitude smaller than that of

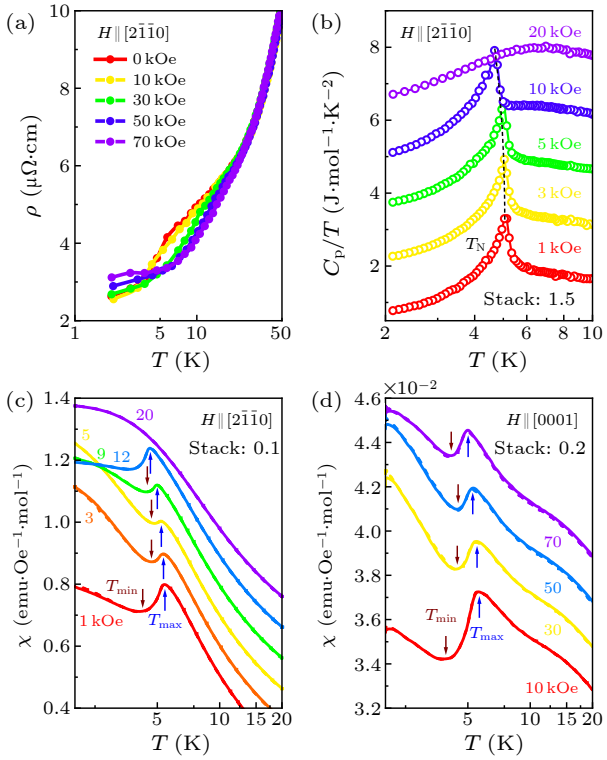

Fig. 4. Magnetic order behavior of Pr_3ScBi_5 measured under varying magnetic fields at low temperatures. (a) Temperature variations of the electrical resistivity for magnetic field parallel to $[2\bar{1}\bar{1}0]$ and the current along c-axis. (b) Low-temperature C_p/T versus T curves with varied magnetic fields for $[2\bar{1}\bar{1}0]$. (c) and (d) Temperature-dependent magnetic susceptibility under various magnetic fields for $[2\bar{1}\bar{1}0]$ and [0001]. The upward blue arrow and the downward purple arrow denote the local maxima and minima of the magnetic susceptibility curves, respectively.

$H \parallel [2\bar{1}\bar{1}0]$, yet it exhibits a similar peculiar behavior. As the field is applied, the transition at T_N shifts to lower temperatures, persisting even at $H = 70$ kOe (more details in $d\chi/dT$ curves can be seen in Fig. S4(c) of the SM). This observation indicates a strong AFM coupling within the Q1D zigzag chains of the Ln_3ScBi_5 system, where spin motion is significantly constrained. Furthermore, we conducted a detailed study of the magnetic properties in the $H \parallel [0\bar{1}10]$ direction, as shown in Fig. S7 of the SM. The numerical values and trends of the magnetic susceptibility are highly consistent with those in the $H \parallel [2\bar{1}\bar{1}0]$ direction, indicating that Pr_3ScBi_5 single crystals exhibit almost no anisotropy within the Q2D kagome plane. This observation holds true for the broader Ln_3ScBi_5 system as well. It inevitably evokes a classic magnetic structure: the Pr^{3+} moments form a non-collinear AFM arrangement within the Pr triangle of Q2D kagome layers, with spins rotated by 120° relative to one another. Additionally, the Pr moments closest to the [0001] direction are antiparallel, giving rise to three Q1D zig-zag steps of AFM coupling at the Pr sites. In a study utilizing powder neutron diffraction on the isomorphic compound Nd_3TiSb_5, a similar 120° AFM order within the kagome plane was reported.[36] This scenario urgently necessitates further analysis and verification through single-crystal neutron diffraction.

3.4. Magnetization, Magnetoresistance and Phase Diagram. The magnetization evolution [Figs. 5(a) and 5(b)] under a magnetic field further reveals the uniaxial anisotropic AFM behavior of Pr_3ScBi_5. When we apply the field parallel to the $[2\bar{1}\bar{1}0]$ direction at 2 K, the in-plane $M(H)$ curve evolves monotonically and exhibits a weak kink near $H_1 \approx 3$ kOe and a sharp rise near $H_{sp} \approx 15.5$ kOe (more details in dM/dH curves can be seen in Fig. S6 of the SM), followed by a nonlinear increase afterwards. This indicates that the initial AFM-2 state changes to the AFM-1 state at H_1, and then to a polarized-ferromagnetic state via a spin-flop transition at H_{sp}. Below T_N, H_1 and H_{sp} shift towards lower fields as the temperature rises (Fig. S6 of the SM). In contrast, the magnetic moment shows a linear field dependence, as expected for an antiferromagnet under out-of-plane fields [Fig. 5(b)]. No indication of magnetization saturation is observed up to 70 kOe for both field orientations. The values of $M(H)$ at 70 kOe at 2 K are 1.38 μ_B/Pr^{3+} ($H \parallel [2\bar{1}\bar{1}0]$) and 1.59 × 10^{-2} μ_B/Pr^{3+} ($H \parallel [0001]$), which are substantially less than the full moment of free Pr^{3+} ion, suggesting the significant role of CEF on the ground-state multiplet.[28,37] These distinct magnetization behaviors offer further confirmation of the in-plane arrangement of Pr magnetic moments, aligning with our previous conjecture about the magnetic structure.

Magnetoresistance (MR) implies some sort of coupling between magnetic order and the electronic structure. In Fig. 5(c), we present the calculated MR [MR (%) = 100 × $[\rho_{\parallel}(H) - \rho_{\parallel}(H = 0)]/\rho_{\parallel}(H = 0)$] at various temperatures, with current directed along the [0001] direction and field aligned parallel to the $[2\bar{1}\bar{1}0]$ direction. At $T = 2$ K, the MR initially exhibits negative MR, and then through the spin-flop transformation, it becomes monotonically increasing until $H_2 = 75$ kOe reaches a maximum positive MR of 15%. Conversely, when the temperature rises to 5 K, the spin-flop transition vanishes (Fig. S6 of the SM), and the MR slightly increases below the H_1 field before transitioning to negative behavior, ultimately achieving a 15% negative MR at 90 kOe. Given the intricate magnetic structure exhibited by Pr_3ScBi_5 and the role of spin-dependent electron scattering, further investigations are essential to fully elucidate the underlying mechanisms governing this MR behavior. As illustrated in Fig. 5(d), by compiling the critical fields and ordering temperatures derived from multiple measurements, we construct the temperature-magnetic field phase diagram of Pr_3ScBi_5 for $H \parallel [2\bar{1}\bar{1}0]$. The phase diagram delineates the AFM ordered phases below 5.1 K and 15.5 kOe, where the AFM1 phase and the AFM2 phase are separated by the field-induced transition marked by the peaks in dM/dH and MR–H at H_1. The phase boundary lines of the AFM phase and possible PFM states in other regions are determined jointly by magnetic transitions from χ–T, ρ–T, and C_p–T measurements, as well as spin-flop transitions observed in M–H and MR data. The transitions and anomalies evident in various measurements highlight the intricate interplay between magnetic order arising from mixing ground and low-lying singlets and the effects of

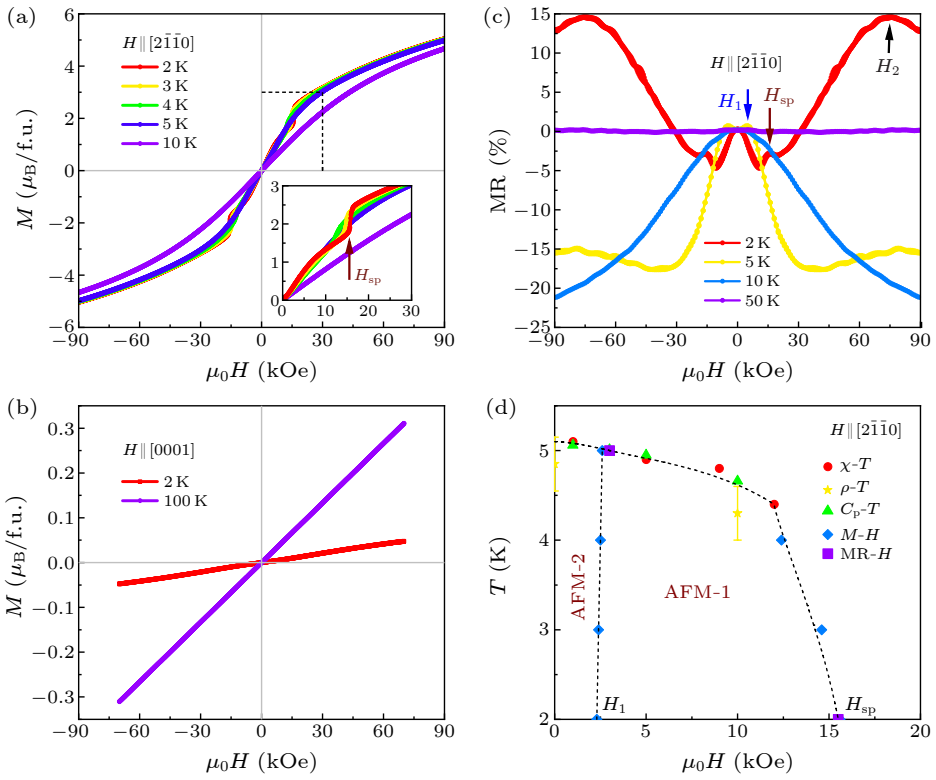

Fig. 5. Field-dependent physical properties and phase diagram of Pr_3ScBi_5. (a) and (b) Isothermal magnetizations under various magnetic fields for $H \parallel [2\bar{1}\bar{1}0]$ and $H \parallel [0001]$. (c) Field dependence of magnetoresistance in the magnetic field up to 90 kOe for $H \parallel [2\bar{1}\bar{1}0]$ at various temperatures. (d) Temperature-magnetic field phase diagram of Pr_3ScBi_5 for $H \parallel [2\bar{1}\bar{1}0]$.

applied magnetic field.[38,39] Investigating the behavior of quantum critical state when thermally induced magnetic order in Ln_3ScBi_5 system is driven to zero remains a compelling subject for future research.

4. Conclusions. The Ln_3ScBi_5 family has emerged as one of the most impactful and chemically versatile kagome platforms, characterized by its robust structural framework and tunable physical properties. This research commenced with a thorough evaluation of the currently known Ln_3ScBi_5 materials, offering a robust methodology for visualizing structural polymorphs and evaluating their stability boundaries within this family. Simultaneously, we successfully optimized the conditions for flux growth synthesis, yielding a series of high-quality single crystals from the Ln_3ScBi_5 family, in which the rare earth atoms exhibited zig-zag chains typical of Q1D motifs and were located within the distorted kagome layers of Q2D networks.

We utilized Pr_3ScBi_5 as the research medium to investigate the intricate magnetic ground states and distinctive transport phenomena arising from the mixed-dimensional structure of the system. Pr_3ScBi_5 exhibits an AFM phase transition at $T_N = 5.1$ K, independent of the magnetic field orientation along the $[2\bar{1}\bar{1}0]$ or [0001] crystallographic directions. Our study reveals that the ordered magnetic moments of Pr^{3+} ions are confined within the Q2D kagome planes, displaying minimal in-plane anisotropy. In contrast, a strong AFM coupling is observed within the Q1D zigzag chains, where spin motion is significantly constrained. This distinctive magnetic structural characteristic is commonly observed across the Ln_3ScBi_5 family of compounds. Furthermore, the substantial reduction in magnetic entropy at T_N compared to $R \ln 2$, along with the observation that AFM phase transitions occur at lower temperatures below the wide peak of magnetic susceptibility, suggests the presence of pronounced spin fluctuations in Pr_3ScBi_5. A plausible mechanism within the Ln_3ScBi_5 system is that the rare earth atoms are sufficiently spaced to preclude direct exchange interactions, and thus the system relies on RKKY-type long-range interactions, which typically cause the impact of a geometrically frustrated lattice. The Ln_3ScBi_5 materials, with their significant structural flexibility, are promising candidates for the emergence of physical states in mixed-dimensional motifs in bulk materials.

Acknowledgements. This work was supported by the National Key R&D Program of China (Grant Nos. 2024YFA1408400 and 2021YFA1400401), the National Natural Science Foundation of China (Grant Nos. U22A6005 and 52271238), the China Postdoctoral Science Foundation (Grant No. 2025M770186), the Center for Materials Genome, and the Synergetic Extreme Condition User Facility (SECUF). The study is also financially supported by the AI-driven experiments, simulations and model training on the robotic AI-Scientist platform from Chinese Academy of Sciences and the Research Funds for the Central Universities (Grant No. N25ZLE007).

References

[1] Liu X, Choi M S, Hwang E, Yoo W J, and Sun J 2022 *Adv. Mater.* **34** 2108425
[2] Maciejko J and Fiete G A 2015 *Nat. Phys.* **11** 385
[3] Liu X and Hersam M C 2019 *Nat. Rev. Mater.* **4** 669
[4] Bao J K, Liu J Y, Ma C W, Meng Z H, Tang Z T, Sun Y L, Zhai H F, Jiang H, Bai H, Feng C M, Xu Z A, and Cao G H 2015 *Phys. Rev. X.* **5** 011013
[5] Faure Q, Takayoshi S, Simonet V, Grenier B, Månsson M, White J S, Tucker G S, Rüegg C, Lejay P, Giamarchi T, and Petit S 2019 *Phys. Rev. Lett.* **123** 027204
[6] Bingham N S, Rooke S, Park J, Simon A, Zhu W, Zhang X, Batley J, Watts J D, Leighton C, Dahmen K A, and Schiffer P 2021 *Phys. Rev. Lett.* **127** 207203
[7] Arnesen M C, Bose S, and Vedral V 2001 *Phys. Rev. Lett.* **87** 017901
[8] Yokoi C S O, Tang L H, and Chou W 1988 *Phys. Rev. B* **37** 2173
[9] Zhong Y, Liu J, Wu X, Guguchia Z, Yin J X, Mine A, Li Y, Najafzadeh S, Das D, Mielke C, Khasanov R, Luetkens H, Suzuki T, Liu K, Han X, Kondo T, Hu J, Shin S, Wang Z, Shi X, Yao Y, and Okazaki K 2023 *Nature* **617** 488
[10] Yang S Y, Wang Y, Ortiz B R, Liu D, Gayles J, Derunova E, Gonzalez-Hernandez R, Smejkal L, Chen Y, Parkin S S P, Wilson S D, Toberer E S, Mcqueen T, and Ali M N 2020 *Sci. Adv.* **6** eabb6003
[11] Chen H, Yang H, Hu B, Zhao Z, Yuan J, Xing Y, Qian G, Huang Z, Li G, Ye Y, Ma S, Ni S, Zhang H, Yin Q, Gong C, Tu Z, Lei H, Tan H, Zhou S, Shen C, Dong X, Yan B, Wang Z, and Gao H J 2021 *Nature* **599** 222
[12] Zhao H, Zhang J, Lyu M, Bachus S, Tokiwa Y, Gegenwart P, Zhang S, Cheng J, Yang Y f, Chen G, Isikawa Y, Si Q, Steglich F, and Sun P 2019 *Nat. Phys.* **15** 1261
[13] Xu Z, Yan Y, Liu Z, Pang J, Dong G, Deng X, Zhang S, Zhang X, Shi Y, and Wu Q 2025 *npj Quantum Mater.* **10** 41
[14] Xu Z, Wang Y, Zhang C, Liu H, Han X, Wu L, Zhang X, Wu Q, and Shi Y 2024 *Phys. Rev. B* **110** 165106
[15] Zhang C, Wang Y, Zheng J, Du L, Li Y, Han X, Liu E, Wu Q, and Shi Y 2024 *Phys. Rev. Mater.* **8** 034402
[16] Zhang C, Pang J, Dong G, Zhang S, Wu Q, Shi Y, and Wang Y 2025 *Phys. Rev. Mater.* **9** 054404
[17] Zelinska O Y and Mar A 2008 *Inorg. Chem.* **47** 297
[18] Han X, Pi H, Yan D, Zhang R, Li Y, Wang X, Dun Z, Wang Z, Feng H L, Wu Q, and Shi Y 2023 *Phys. Rev. B.* **108** 075157
[19] Han X, Li Y, Yang M, Miao S, Yan D, and Shi Y 2023 *Phys. Rev. Mater.* **7** 124406
[20] Khoury J F, Han B, Jovanovic M, Singha R, Song X, Queiroz R, Ong N P, Schoop L M 2022 *J. Am. Chem. Soc.* **144** 9785
[21] Murakami T, Yamamoto T, Takeiri F, Nakano K, and Kageyama H 2017 *Inorg. Chem.* **56** 5041
[22] Khoury J F, Song X, and Schoop L M 2022 *Z. Anorg. Allg. Chem.* **648** e202200123
[23] Motoyama G, Sezaki M, Gouchi J, Miyoshi K, Nishigori S, Mutou T, Fujiwara K, and Uwatoko Y 2018 *Physica B.* **536** 142
[24] Motoyama G, Shinozaki M, Tsubouchi M, Kuninaka M, Nishigori S, Miyoshi K, Fujiwara K, Gouchi J, and Uwatoko Y 2020 *JPS Conf. Proc.* **30** 011180
[25] Ortiz B R, Miao H, Parker D S, Yang F, Samolyuk G D, Clements E M, Rajapitamahuni A, Yilmaz T, Vescovo E, Yan J, May A F, and Mcguire M A 2023 *Chem. Mater.* **35** 9756
[26] Šibav L, Lozinšek M, Jagličić Z, Arh T, Khuntia P, Zorko A, and Dragomir M 2025 *Cryst. Growth Des.* **25** 4646
[27] Chen K W, Lai Y, Chiu Y C, Steven S, Besara T, Graf D, Siegrist T, Albrecht-Schmitt T E, Balicas L, and Baumbach R E 2017 *Phys. Rev. B.* **96** 014421
[28] Sakai A and Nakatsuji S 2011 *J. Phys. Soc. Jpn.* **80** 063701
[29] Ernst S, Kirchner S, Krellner C, Geibel C, Zwicknagl G, Steglich F, and Wirth S 2011 *Nature* **474** 362
[30] Yan D Y, Yang M, Song P B, Song Y T, Wang C X, Yi C J, and Shi Y G 2021 *Phys. Rev. B* **103** 224412
[31] Kusanose Y, Onimaru T, Park G-B, Yamane Y, Umeo K, Takabatake T, Kawata N, and Mizuta T 2019 *J. Phys. Soc. Jpn.* **88** 083703
[32] Pathak A K, Paudyal D, Mudryk Y, Gschneidner K A, and Pecharsky V K 2013 *Phys. Rev. Lett.* **110** 186405
[33] Maurya A, Kulkarni R, Thamizhavel A, Paudyal D, and Dhar S K 2016 *J. Phys. Soc. Jpn.* **85** 034720
[34] Wang Z, Zhao H, Lyu M, Xiang J, Isikawa Y, Zhang S, and Sun P 2022 *Phys. Rev. B* **105** 125113
[35] Ishii H 2004 *J. Low Temp. Phys.* **135** 579
[36] Ritter C, Pathak A K, Filippone R, Provino A, Dhar S K, and Manfrinetti P 2021 *J. Phys.: Condens. Matter* **33** 245801
[37] Onimaru T, Nagasawa N, Matsumoto K T, Wakiya K, Umeo K, Kittaka S, Sakakibara T, Matsushita Y, and Takabatake T 2012 *Phys. Rev. B.* **86** 184426
[38] Nair H S, Ghosh S K, Ramesh Kumar K, and Strydom A M 2016 *J. Phys. Chem. Solids* **91** 69
[39] Garcia F A, Kumari S, Schmidt J, Adriano C, Sapkota A, Canfield P C, Flint R, and Ribeiro R A 2025 *Phys. Rev. B.* **111** 245160